Available online at www.sciencedirect.com

SciVerse ScienceDirect

Acta Materialia 60 (2012) 4393–4408

Acta MATERIALIA

www.elsevier.com/locate/actamat

Microstructure, texture and mechanical properties of aluminum processed by high-pressure tube twisting

M. Arzaghi [a], J.J. Fundenberger [a,b], L.S. Toth [a,b,*], R. Arruffat [a,b], L. Faure [a,b], B. Beausir [a,b], X. Sauvage [c]

[a] Laboratoire d'Etude des Microstructures et de Mécanique des Matériaux (LEM3), CNRS UMR 7239, Université de Lorraine, Metz, France

[b] Laboratory of Excellence on Design of Alloy Metals for low-mAss Structures (DAMAS), Université de Lorraine, France

[c] University of Rouen, Groupe de Physique des Matériaux, CNRS UMR 6634, Saint-Etienne du Rouvray, France

Received 7 January 2012; received in revised form 26 April 2012; accepted 27 April 2012

Abstract

The new severe plastic deformation technique known as high-pressure tube twisting (HPTT) is a continuous process to obtain grain refinement in bulk metallic materials of tubular geometry. HPTT was applied to commercially pure aluminum up to a shear strain of 24. The mechanical properties were enhanced markedly and were characterized by compression and ring-hoop tensile tests. It was shown that the axial force during HPTT does not contribute to the plastic flow of the material; it is only controlled by the shear component of the applied stress. The microstructure and the crystallographic texture were examined in detail by electron backscatter diffraction, transmission electron microscopy, and X-ray diffraction, and these showed the existence of a gradient within the cross-section of the tube. The next-neighbor grain misorientation distribution showed a bimodal nature, of which the small-angle peak was attributed to the "internal" new grains originating from the interior of the initial grains and the second one from the new grains situated at the grain boundaries of the initial grains. The measured textures were typical shear textures with specific tilts in the sense of the shear direction at large strains, which can be attributed to the effect of strain rate sensitivity of slip. The main component of the textures was the C component, which continuously strengthened with the shear. The results obtained suggest that HPTT is an efficient processing way to transform the microstructure of Al tubes into ultra-fine-grained structures in one single operation.

Keywords: Severe plastic deformation; Grain refinement; Microstructure; Texture; High-pressure tube twisting

1. Introduction

Obtaining large plastic deformation is quite complicated in most classic metal forming processes as it can become finally limited by either material or tool failure. Severe plastic deformation (SPD) techniques offer the advantage of imparting the strain under compressive stress state, thus deferring structural damage until large strains are applied. Therefore, SPD has become a progressing direction of research in nanoscience and nanotechnology for industrial production of ultra-fine-grained (UFG) metals with enhanced mechanical or functional properties. Those properties are: high strength at ambient temperature and high-speed superplastic deformation at elevated temperatures. The resulting submicrometer grain structures are generally known as "nano-SPD" or bulk nanostructured (BNM) materials [1]. Up to now, the most widely used SPD processes are equal channel angular extrusion (ECAE) [2–5], high-pressure torsion (HPT) [6], and accumulated roll bonding (ARB) [7]. Among these three processes HPT is a continuous process; however, the samples are small and there is a strain inhomogeneity through the radial direction which is not desirable for practical applications. Inhomogeneities may exist even across the thickness of the disk [8].

* Corresponding author at: Laboratoire d'Etude des Microstructures et de Mécanique des Matériaux (LEM3), CNRS UMR 7239, Université de Lorraine, Metz, France. Tel.: +33 387315361; fax: +33 387315366.

E-mail address: toth@univ-metz.fr (L.S. Toth).

1359-6454/$36.00
http://dx.doi.org/10.1016/j.actamat.2012.04.035

High-pressure tube twisting (HPTT) [9] is a new SPD method proposed for manufacturing high-strength thin-walled tubes and cylinders to obtain net-shaped engineering components. In HPTT a tube is positioned on a mandrel and then fully constrained by another mandrel from the top, see Fig. 1. The tube is then confined by applying a compression force on its upper and bottom wall surfaces, leading to a small axial shortening of the sample. The force is sufficiently large to form protrusions along the tube on the top and bottom surfaces which lead to a high hydrostatic pressure in the entire volume of the tube. This hydrostatic stress is necessary to create large friction forces on both sides of the testing tube. Finally, the deformation of the tube is achieved by rotating the external lateral surface of the tube with a torque that is applied on the twisting mandrel while keeping the internal lateral surface of the tube immobile with the fixed mandrel. During the twisting a shear deformation develops within the wall of the tube where the shear plane normal is radial and the shear direction is tangential to the tube. There is no deformation in the axial direction during twisting.

Another SPD process suitable for tubes was also proposed [10] in which the tube is pushed through a tubular die containing a ring-type zone where it can be deformed locally (tube channel pressing). It seems, however, that that process is technically difficult to put into operation. There are several other new propositions to perform SPD on materials [11,12].

It should be noted that Bridgman has also tried twisting tubes under axial pressure [13]. However, his setup was fundamentally different from the present HPTT testing. Deformation was taking place only in two narrow pre-notched places of the tube and shear was applied as in torsion, that is, in the plane perpendicular to the axis of the tube. In HPTT the shear plane is tangential to the tube wall and deformation is driven by friction force.

It was found experimentally [9] that the shear strain is not constant within the tube wall; it is maximal at the inner wall and decreases monotonically towards the external wall; this gradient is opposite to the gradient during HPT where the strain is increasing with the radius. The following formula relates the rotation angle θ of the rotating mandrel to the shear distribution $\gamma(r)$:

$$\theta = \int_a^b \frac{\gamma(r)}{r} dr \tag{1}$$

Here a and b are the internal and external radii of the tube, respectively. An average shear strain $\bar{\gamma}$ can be calculated to characterize the strain state in the tube by replacing $\gamma(r)$ with $\bar{\gamma}$ in Eq. (1) and integrating:

$$\bar{\gamma} = \frac{\theta}{\ln(b/a)} \tag{2}$$

For a geometry of $b/a = 10/9$, and for one turn, Eq. (2) gives $\bar{\gamma} = 9.49 \times 2\pi = 59.64$, which is an extremely large strain. Note that such a large strain can be achieved by HPT only in the outer radius of the disk if its diameter-to-thickness ratio is 19. Not only the shear strain but also the shear stress has a gradient within the tube. To obtain the variation of the shear stress as a function of the radial position within the tube we can write the equilibrium of torques produced by the local shear stress $\tau(r)$ and the external torque T:

$$T = 2r\pi hr\tau(r) \tag{3}$$

Here h is the height of the tube. This relation gives the shear stress variation within the tube wall:

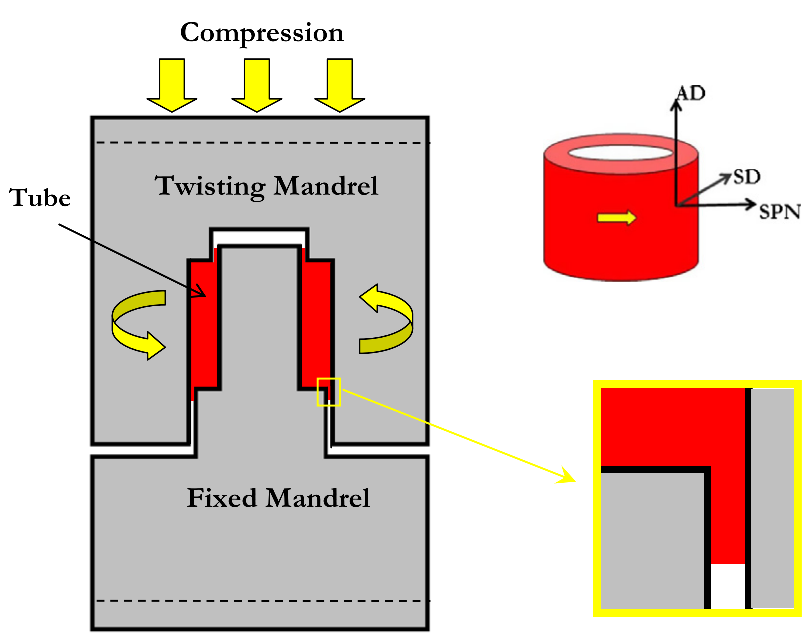

Fig. 1. Schema of the high-pressure tube twisting (HPTT) set-up.

$$\tau(r) = \frac{T}{2r^2\pi h} \tag{4}$$

The shear stress is larger at the internal ($\tau(a)$) than at the external wall ($\tau(b)$); however, its ratio depends only on the geometry:

$$\frac{\tau(a)}{\tau(b)} = \left(\frac{b}{a}\right)^2 \tag{5}$$

For example, for $b/a = 10/9$, $\tau(a)/\tau(b) = 1.23$. Having an average shear strain quantity given by Eq. (2), an average shear stress $\bar{\tau}$ can also be defined. For this purpose we write an increment of plastic work in the volume V of the tube during a rotation of $\Delta\theta$ using the equivalent quantities and the external work increment:

$$\Delta W = T\Delta\theta = \int_V \bar{\tau}\Delta\bar{\gamma}dV = \bar{\tau}\Delta\bar{\gamma}(b^2 - a^2)\pi h \tag{6}$$

This relation, with the help of Eq. (2), provides an appropriate measure for the average shear stress:

$$\bar{\tau} = \frac{T\ln(b/a)}{(b^2 - a^2)\pi h} \tag{7}$$

It is then possible to plot stress–strain curves for the HPTT test using the average shear strain and average shear stress quantities given by Eqs. (2) and (7), respectively. It is also possible to obtain the shear strain distribution in an analytical way; for such an analysis, see Ref. [14].

Apparently there is no limit to the amount of shear in this process, so the grain refinement procedure can be very efficient. HPTT outperforms HPT in its geometrical aspect as tubes are very frequently used in practical applications and because it has the potential for scaling up to produce relatively large samples.

The present work focuses on the recent results obtained with a new facility developed for performing HPTT. Tubes of commercially pure (CP) aluminum were deformed up to a shear strain of 24. Microstructure was studied by electron backscatter diffraction (EBSD) and transmission electron microscopy (TEM), and crystallographic texture was examined by X-rays. The mechanical properties were characterized thanks to stress–strain curves measured during HPTT as well as compression and ring-hoop tensile testing. The results show that HPTT is a very efficient technique to obtain UFG microstructures with enhanced mechanical properties.

2. Experimental procedures

2.1. Material

Tubes were machined from CP aluminum A1050 bars with dimensions of inner and outer diameters of 18 and 20 mm and a height of 8 mm. This relatively short tube geometry was selected because of the limitations in the torque capacity of our testing device. Before the test, the tubes were heat-treated at 400 °C for 20 min and then water-quenched, resulting in equiaxed grains with an average size of ~24 μm with quite large dispersion around this value; see the grain structure in Fig. 2.

2.2. Processing by HPTT

HPTT processing of Al tubes was conducted at room temperature under a quasi-hydrostatic pressure of ~1 GPa using the setup illustrated schematically in Fig. 1. In order to study the evolution of the stress as a function of average shear strain $\bar{\gamma}$, the torque was monitored as a function of twist angle. The compression force was measured electronically but was adjusted manually to keep the hydrostatic pressure nearly constant throughout the process. Tests were done for shear strains up to 24, at room temperature. The applied shear rate was 0.1 s^{-1}.

2.3. Mechanical testing after HPTT

After HPTT processing, the mechanical properties were examined by tensile and compression tests (see Fig. 3). To obtain tensile properties of the tubular samples, ring-hoop tension testing [15] was chosen. It is indeed the most appropriate technique for tubes with small dimensions or with low formability. Fig. 3a shows the configuration of the test as well as the sample dimensions. The reduced section area of the tubes was placed on the top D-block that is at $\theta = 90°$ and the contact surfaces were lubricated with Teflon spray to reduce friction effects. Compression tests were performed at room temperature directly on the tubes placed between two flat plates at a constant displacement rate (Fig. 3b). All tests were performed with a cross-head speed of 0.5 mm min^{-1}, producing an initial strain rate of 1.3×10^{-3} s^{-1}.

2.4. Texture measurements

Textures developed by HPTT were measured using a home-made texture goniometer with a Cu tube using the X-ray diffraction method on the lateral surface of the tube. The sample reference system consisted of the shear direction (SD), the shear plane normal (SPN) and the axial direction (AD), see Fig. 1. To prepare a flat surface required for the measurements, the tubes were first cut into two parts vertically across their diameter, and were then flattened. To minimize the introduced strains while flattening the surface, the tubes were chemically thinned to half thickness using a solution of 40% NaOH for ~6 h. With the help of a compression machine, a force of ~100 N was applied on the curved surface for flattening. It should be noted that due to this operation a negligible small deformation was imparted to the specimen. However, it is believed that it should not significantly change the texture. The supplementary strain is a shear which can be estimated to be $\gamma = t/b = 0.25$ mm/8 mm = 0.031, where t is the thickness and b is the outer radius of the tube. Four pole figures ({1 1 1}, {2 0 0}, {2 2 0}, {3 1 1}) were measured, from which the orientation

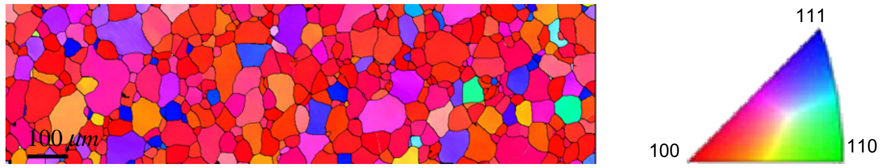

Fig. 2. Inverse pole figure map of the grain structure before HPTT obtained by EBSD. The projected direction is the axial direction of the tube.

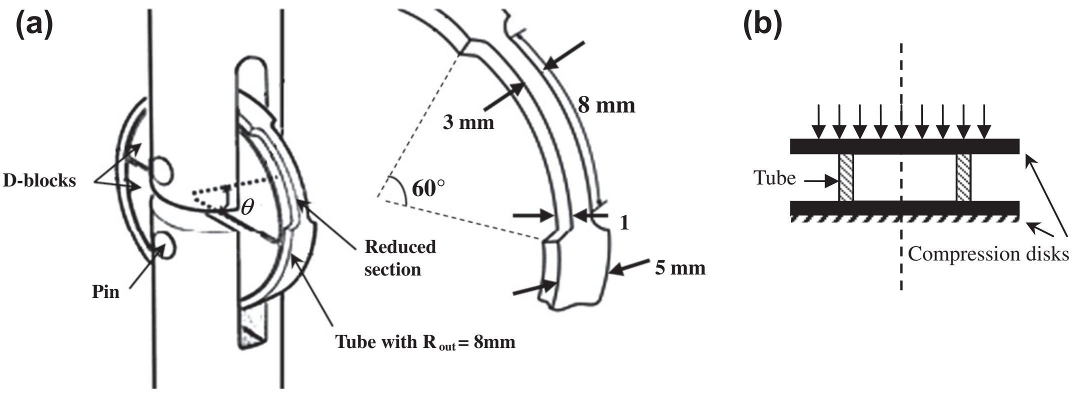

Fig. 3. Schematic configuration of (a) ring-hoop tensile and (b) compression samples with the compression axes lying parallel to the longitudinal axes of the tube.

distribution function (ODF) was determined using the texture software developed at the laboratory LEM3.

2.5. Microstructure studies

The microstructure was examined using the EBSD technique and by transmission electron microscopy (TEM). The EBSD investigations were performed on the AD plane using a JEOL 6500F field emission gun scanning electron microscope (FEG-SEM) equipped with HKL acquisition software operating at 15 kV. The sample preparation for EBSD was done first by mechanical grinding on wet SiC paper (grit 500–4000) followed by alumina solution of 0.8 μm and 0.25 μm. A final electropolishing to a mirror-like surface was accomplished using an electrolyte of 20% perchloric acid and 80% ethanol at 258 K and a DC voltage of 18 V. The EBSD observations were done with different step sizes; 1.2, 0.6, 0.3 or 0.06 μm depending on the studied zone. The measured areas were located within the tube wall near to its inner surface, in the middle and near to the outer surface. These observations allowed us to analyze quantitatively the grain/subgrain structures as small as $\sim$ 0.2 μm.

In order to determine grain sizes with EBSD, a grain was defined by using two criteria. The first one was based on a minimum number of data points per grain, while the second used the threshold boundary misorientation angle. Concerning the first criterion, it is reported that eight measurement points across a grain correspond to an accuracy of 5% [16] in the obtained grain size, so this criterion was applied in the present study. The threshold boundary misorientation angle is equally critical in estimating grain size. Based on the resolution limit of the EBSD system, low-angle grain boundaries (LAGBs) were defined by a minimum disorientation angle of 5° between adjacent pixels while high-angle grain boundaries (HAGBs) were identified using a minimum of 15°.

For the sample deformed to the shear strain of 20, TEM studies were conducted using a JEOL 2000FX microscope operated at 200 kV. The samples were taken from the lateral surface of the tube (SPN plane) as well as on its thickness (AD plane). Thin foils were prepared by a twin-jet polishing unit using a solution of 1:3 nitric acid–methanol at 243 K.

3. Results and discussion

3.1. Strain hardening during HPTT

Typical stress–strain curves obtained by HPTT in CP Al are displayed in Fig. 4. The average shear stress calculated by Eq. (7) is plotted in this figure as a function of the average shear (Eq. (2)) together with the axially imposed stress. The latter was obtained by dividing the applied force by the cross-section of the tube wall. Its oscillating nature is due to the manual control of the axial force. Fig. 4 shows the strain-hardening curve up to a shear of 24, during which there was unloading three times (after 60° rotation each time due to limitation in the rotation angle in the equipment). It must be emphasized at this point that the measured torque must have been influenced by the protrusions that developed progressively during the HPTT test. They were extending more and more in the axial direction and increased the surface contact between the sample and the external mandrel. The lengths of the protrusions were in the mm range and

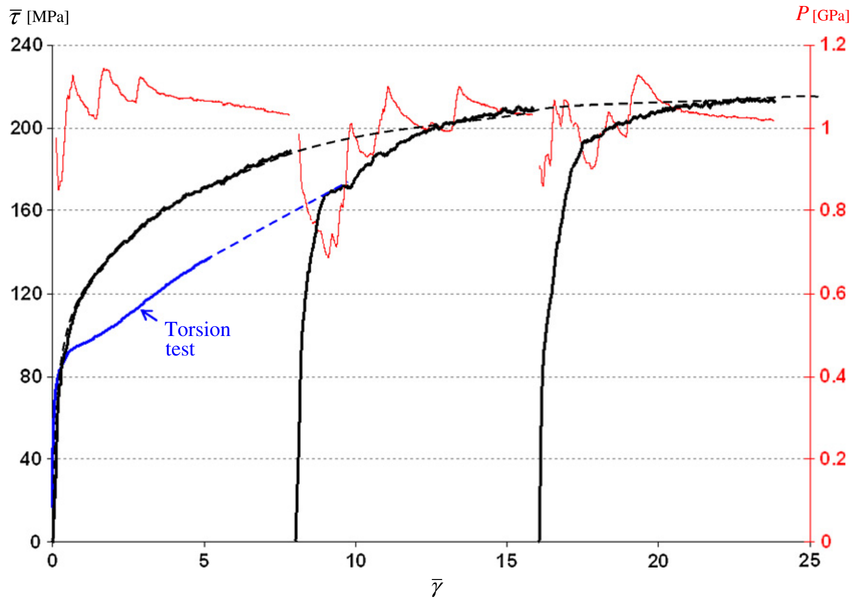

Fig. 4. Stress–strain curves obtained by HPTT for CP Al in three consecutive loadings up to a shear of 24; the upper dashed line envelopes three curves. The strain-hardening curve obtained by free end torsion is superposed for comparison.

were constantly increasing with the rotation. This is why the measured torque was certainly larger than required to deform the tube plastically without the protrusions. For these reasons, the stress data obtained by using Eq. (7) cannot be used in a reliable manner to calculate the average shear stress during the HPTT test and the stress–strain curve plotted for HPTT in Fig. 4 overestimates the real shear flow stress at large strains. A curve enveloping the three hardening curves is also plotted in Fig. 4 to show the transition stages in the strain hardening. The protrusions were removed from the sample before reloading. This explains why there is a significant drop in the flow stress upon reloading with respect to its value before unloading.

For comparison, the strain-hardening curve was also measured by conventional torsion and plotted in Fig. 4. The torsion was carried out on a solid bar (65 mm in length and 6 mm in diameter) in a so-called free-end torsion testing device, at room temperature. Free-end means that the length of the sample could change during torsion (no axial force was applied) and actually a small shortening was observed (3.8% up to a shear of 5). The shear stress was calculated from the torque at the surface of the bar using the Nadai formula [17]. One can see in Fig. 4 that the torsion stress–strain curve lies under the HPTT hardening curve. However, an extrapolation of the torsion curve seems to agree with the flow stress in HPTT after the first reloading (see the broken line extrapolating the torsion curve in Fig. 4). As explained above, the protrusions were removed before reloading the sample, thus the measured HPTT flow stress should be a correct value and it is in agreement with the torsion flow stress. This is the case also at the starting point of both tests where the flow stresses are equal. This agreement means that the flow stress in HPTT is the same as the flow stress in torsion. Consequently, there is no contribution of the axial stress to the plastic flow criterion so that the flow stress is independent of the axial pressure. This characteristic of the HPTT test is theoretically proved in Ref. [14].

An apparent increase of the hardening capacity as a function of the applied compression stress was observed in HPT in Ref. [15] and was interpreted by the effect of the hydrostatic stress on vacancy activation. However, it might be that the stress increase was partially due to the increasing protrusions during those HPT tests, just like in the present HPTT experiments. Kim et al. reported that the protrusions can be very large as a function of the compression load [19], which is accompanied by a significant decrease in the thickness of the HPT samples. (Note also that during HPT, the pressure is usually much larger (~5 GPa).)

3.2. Mechanical properties after HPTT

Fig. 5 shows the engineering stress–strain curves obtained by the ring-hoop tensile test of our CP Al in its initial state and after increasing amounts of shear by HPTT. As can be seen, the yield stress increases with increasing pre-strain while the total elongation decreases. These observations are very similar to those obtained by ECAE on CP Al [20–23]. The onset of necking is indicated on the stress–strain curves using the Considère criterion: $d\sigma/d\varepsilon = \sigma$. These points identify the end of uniform elongation stage, which is drastically reduced after HPTT. The major characteristics of the tensile tests are summarized in Fig. 6, which displays the yield stress, ultimate tensile stress, uniform elongation and total elongation before fracture. After a shear of 2 the uniform elongation drops from its initial 20% value to 2% only. During further shear the

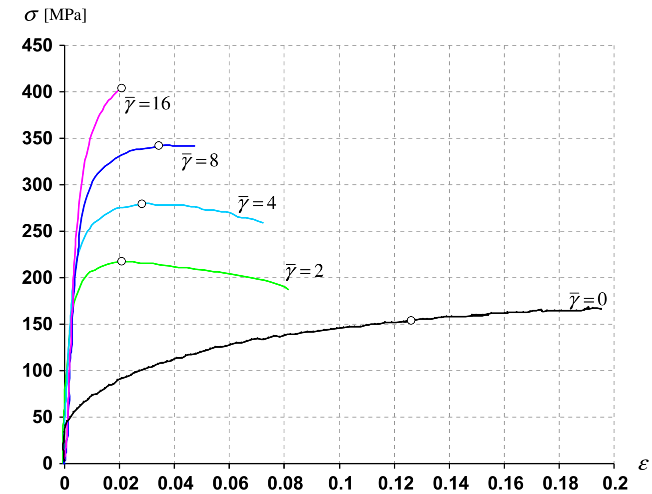

Fig. 5. Tensile true stress–true strain curves obtained by ring-hoop tests of the CP Al tubes processed by HPTT to different amounts of shear strain. Open circles indicate the point of onset of necking according to the Considère criterion.

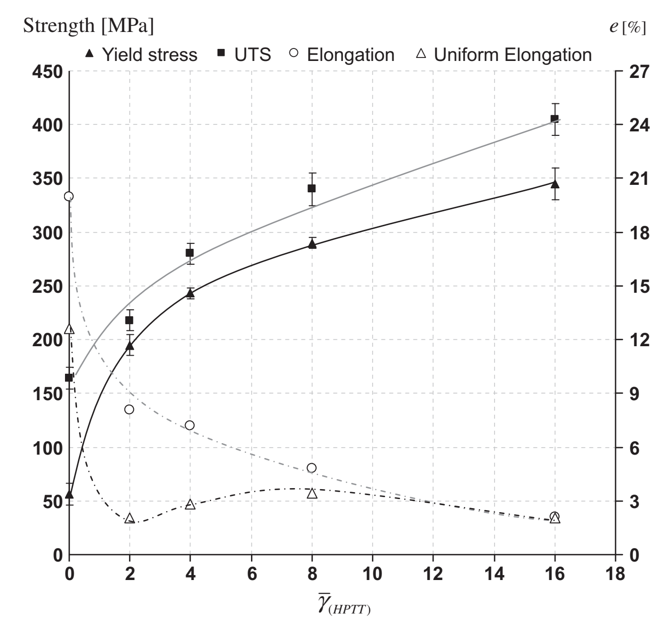

Fig. 6. Development of the tensile properties of tubes processed by HPTT as a function of the pre-strain in HPTT.

uniform elongation increases up to 3.5% at a shear of 8, then decreases again down to 2% at very large shear. The gain in strength, however, is very significant, which is one of the main objectives of SPD deformation processes.

The yield stress measured after HPTT in tension can be converted into shear flow stress using the von Mises criterion, which predicts a shear flow stress $\sqrt{3}$ times smaller than the tensile stress. After unloading at a shear of 8, the tensile flow stress is 290 MPa (see Fig. 6) which gives a shear flow stress of 167 MPa. This value agrees well with the flow stress after reloading, see Fig. 4. Similar good agreement can be seen after a shear of 16; 340 MPa in

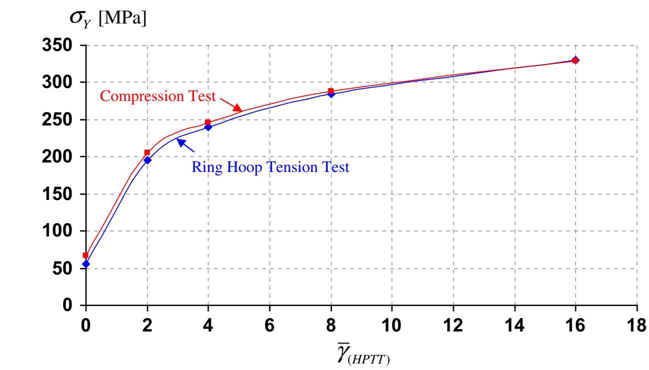

Fig. 7. Comparison between the yield stresses obtained by compression and ring-hoop tests of the HPTT processed CP Al tubes.

tension, which gives 196 MPa in HPTT. These results further support the conclusion made in the preceding section, namely, the plastic flow in HPTT is only provided by the shear stress; the axial stress does not contribute to the yielding. Actually, any contribution from the axial stress should decrease the amplitude of the shear stress below the values predicted from the von Mises yield condition, which is not the case in the present experiments.

Fig. 7 displays the yield strength obtained by tensile as well as by compression tests after HPTT. Stages III and IV are clearly visible in these hardening curves, with Stage IV starting at a shear of ~3. The tensile and compression curves are very similar, which proves the pertinence of the ring-hoop test for measuring tensile strengths of tubular specimens.

As can be seen from our flow stress measurements, the yield stress after HPTT is unusually high considering that we have studied CP aluminum, not an alloy. Indeed, reported values on CP Al do not exceed 200 MPa after SPD (see for ECAP in Refs. [21–23]). The main difference between HPTT and ECAP is the monotonic nature of the HPTT test. During multi-pass ECAP the strain path is changing, even in Route A where grain orientations are rotated by 90° with respect to the shear process. Strain path change always shifts the strain-hardening curve down by a couple of percents with respect to monotonic straining [24]. After several passes in ECAP, the difference is expected to be very significant. The application of a large axial stress also enhances strain hardening, as was shown by Zehetbauer et al. [18] for HPT. According to Rollett [24], the rate of Stage IV hardening normalized by the shear modulus in CP Al on average is $\sim 5.4 \times 10^{-4}$, which is near to the average rate of 5.96×10^{-4} that we can obtain from our measurements (from Fig. 7, between $\gamma = 3$ and 16).

3.3. Microstructural evolution during HPTT

Fig. 8 shows typical EBSD maps taken from the middle zone of the thickness of the tube after processing by HPTT to shear strains of 2, 4 and 8. The colors correspond to the AD direction within the grains as denoted by the unit

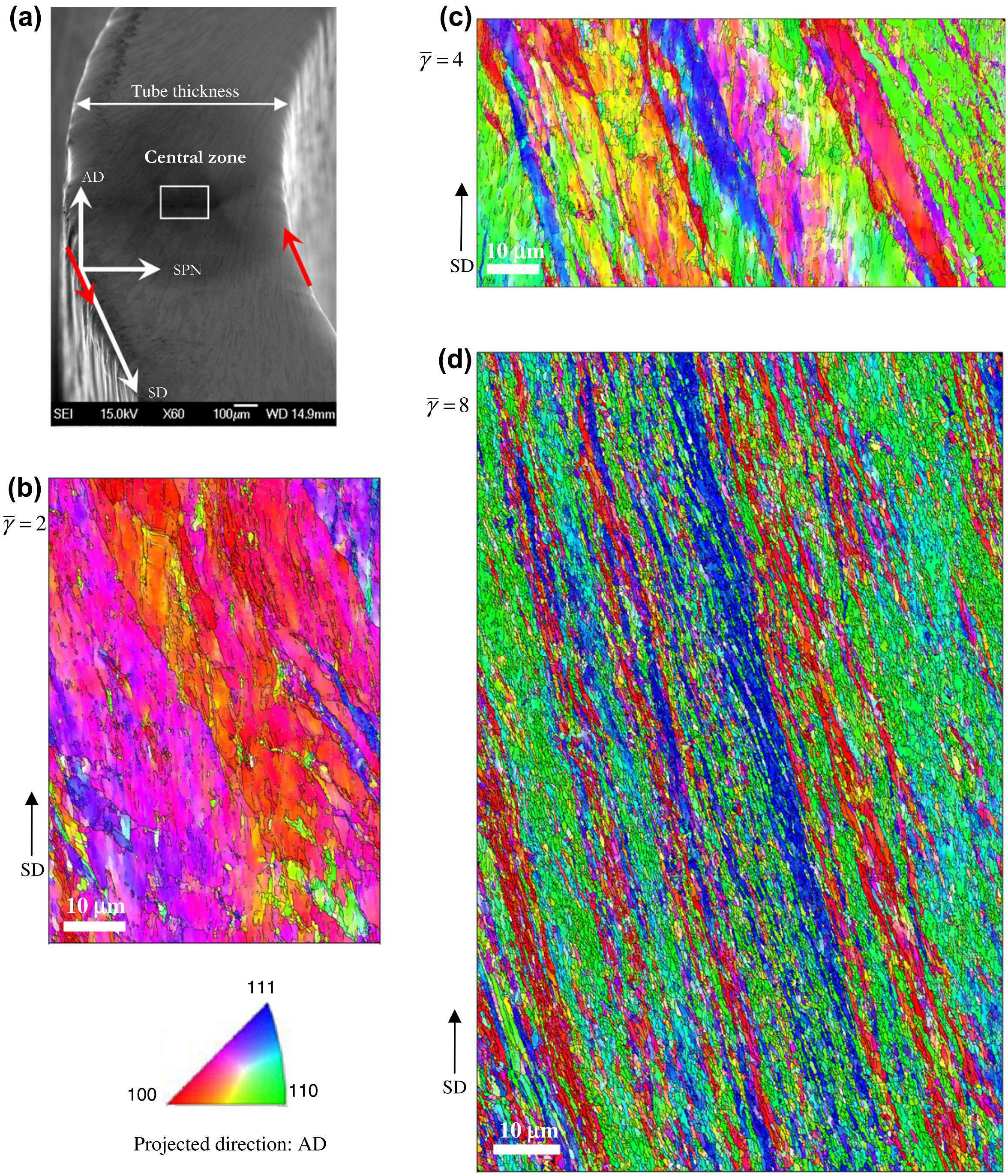

Fig. 8. EBSD maps of CP Al in the middle zone of the thickness of the tube deformed by HPTT to $\bar{\gamma} = 2$ (b), $\bar{\gamma} = 4$ (c) and $\bar{\gamma} = 8$ (d). HAGBs are identified with black lines. Measurement step size: 60 nm.

triangle at the lower left. The image in Fig. 2 shows the material in the unprocessed condition with a typical coarse-grained microstructure. Measurements gave an average grain size of ~ 24 μm for this condition. After a twist of 15° – which corresponds to an imposed shear of $\bar{\gamma} = 2$ – the occurrence of grain fragmentation is visible (Fig. 8b). An important feature of the microstructure in Fig. 8b is that it contains a large number of small- and large-angle boundaries that are parallel to the imposed shear direction.

After a shear of $\bar{\gamma} = 4$ (Fig. 8c), the map is similar in appearance to the previously examined map. Closer inspection reveals, however, strong color differences within the banded structures which are indicative of the presence of increasing orientation differences within grains. These bands appear elongated parallel to the shear direction. Consequently, we can clearly observe a tendency for the new grain boundaries to be formed parallel to the shear direction. Original grains are elongated according to the shear direction and their thickness is about ten times smaller than their

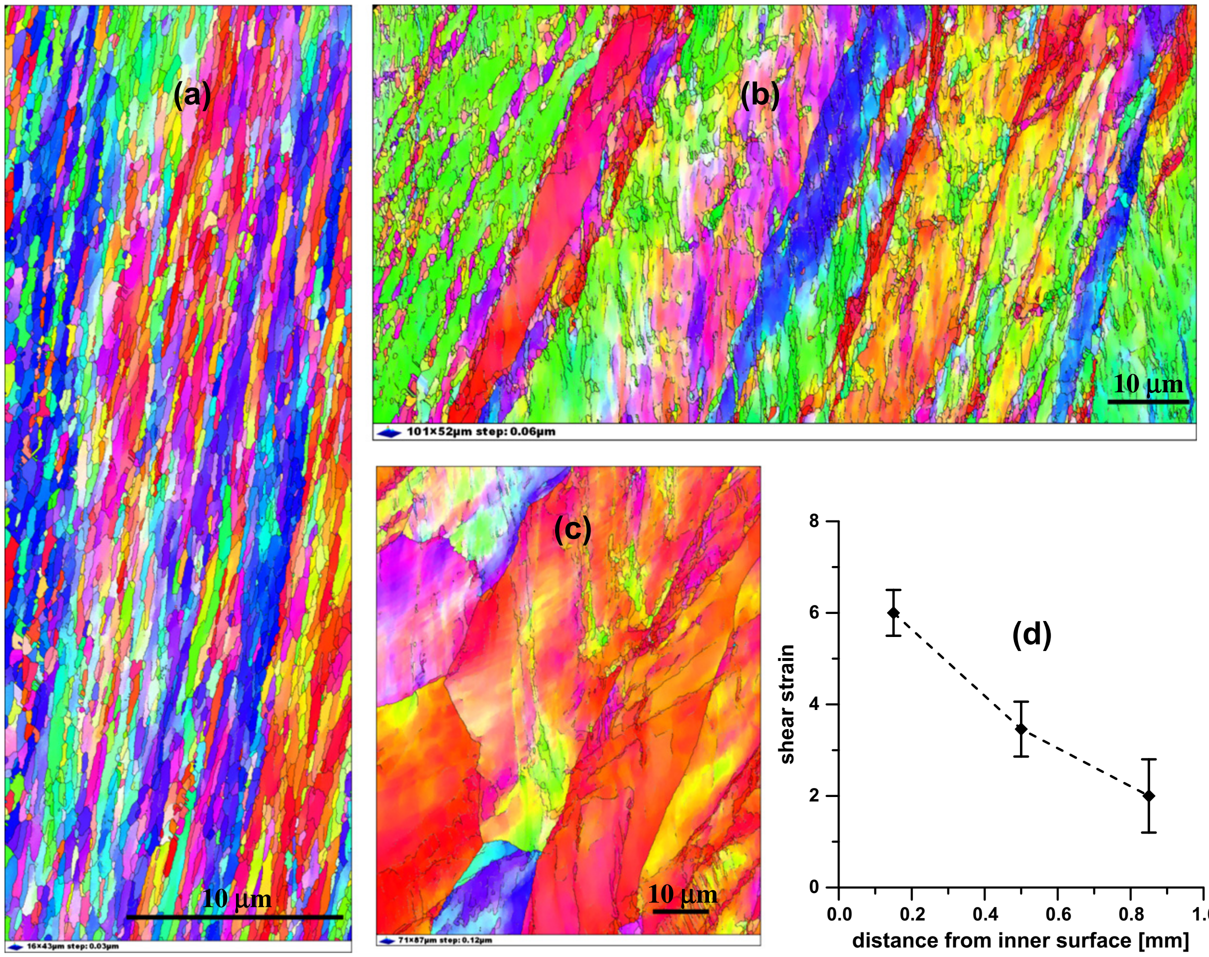

Fig. 9. Micrographs obtained by EBSD after an average shear of ~4 imposed on the tube near the inner surface (a), in the middle (b) and near the outer surface (c). The shear values measured form the three micrographs are displayed in (c) as a function of the distance from the inner surface.

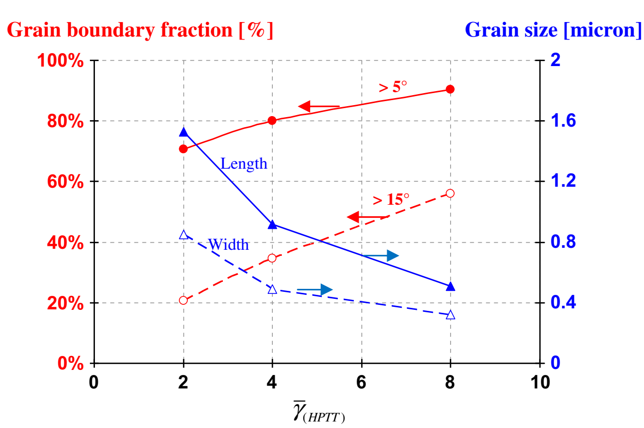

Fig. 10. Evolution of the grain length and width and proportion of HAGB during HPTT of CP Al at room temperature. The grain sizes were obtained by the linear intercept method in two directions: parallel ("length") and perpendicular to the shear direction ("width").

length, with original grain boundaries still distinguishable. The widths of these bands were on average ~3 µm at this stage of the process.

At the shear of $\bar{\gamma} = 8$, the original grains are not recognizable any more (Fig. 8d). This EBSD map confirms the potential of HPTT for introducing an ultra-fine-grained microstructure in pure Al with grains separated by high-angle boundaries and with a final average grain size less than 0.5 µm.

As mentioned in Section 1, the existence of a strain gradient was reported in our previous works [9,14]. Detailed reasons and an analytic modeling for this gradient were presented in Ref. [14]. We have observed similar strain gradients in the present study as well. For illustration and quantitative analysis, Fig. 9 shows three micrographs taken at the internal (a), in the middle (b) and in the outer section (c) of the tube after an average imposed shear of $\bar{\gamma} = 4$ (30° rotation). One can clearly see that the grain structure seems much more deformed in the internal section than in the middle and especially compared with the outer section, where it is much less deformed. The initially equiaxed grains (see Fig. 2) become elongated due to shear and the orientation of the elongated original grain boundaries can be used for an estimation of the local shear strain. At very large strains the original grain boundaries cannot be identified but they must be present (if recrystallization did not take place) so that the new grains have common boundaries with the original grain boundaries. (This effect

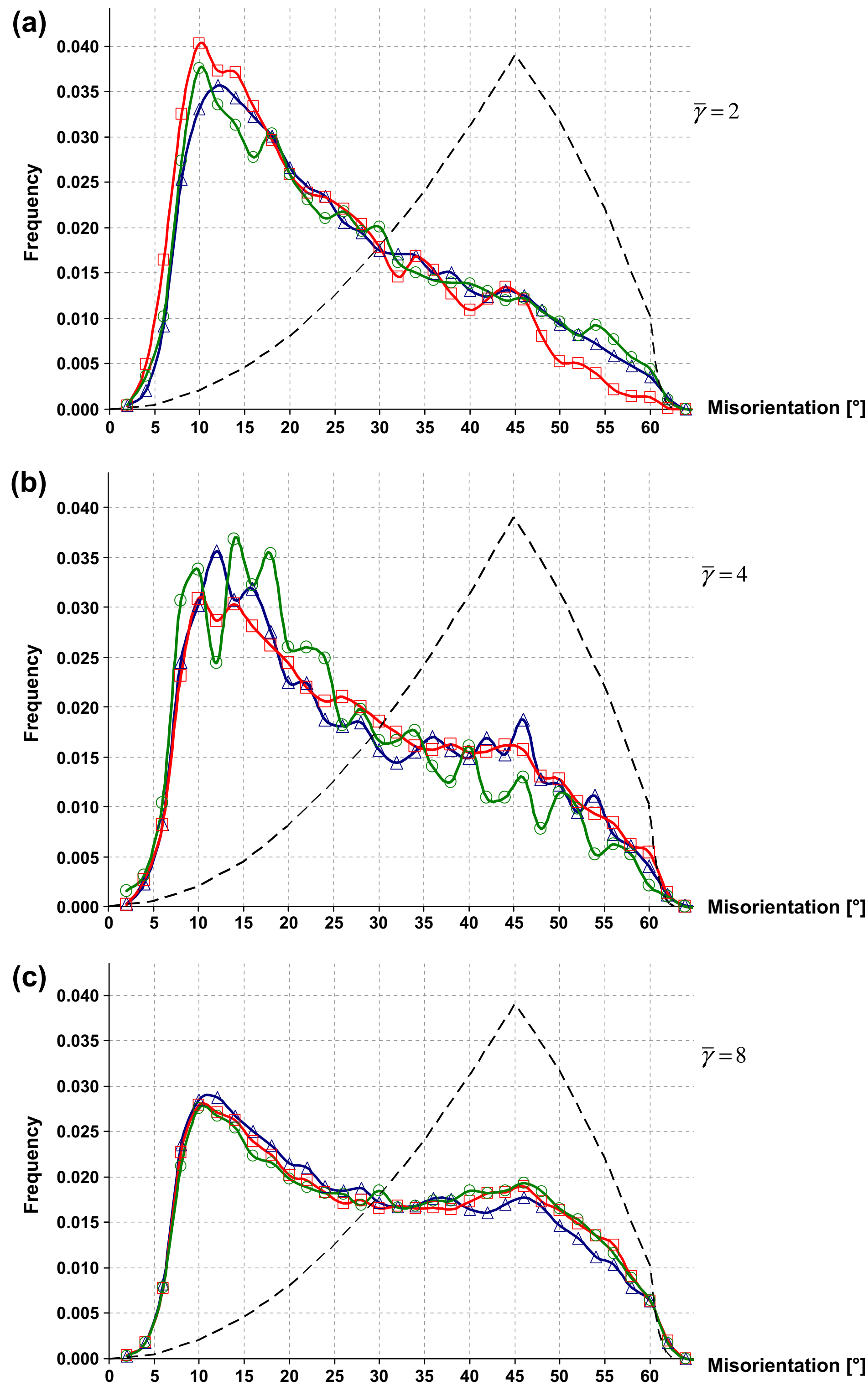

Fig. 11. Next neighbor grain-misorientation distribution for CP Al tubes deformed by HPTT to $\bar{\gamma} = 2$ (a), 4 (b) and 8 (c). Blue line (triangles) corresponds to the inner surface zone, red (squares) to middle zone and green (circles) to the outer surface zone. (For interpretation of the references to color in this figure legend, the reader is referred to the web version of this article.)

makes this analysis less certain in the internal region where Fig. 9c shows high grain fragmentation.) Assuming an initially spherical grain shape, the circular form becomes an ellipse and the measured angle α of the large axis of the elliptic grain with respect to the tangent can be used to obtain the shear strain using the formula [25]:

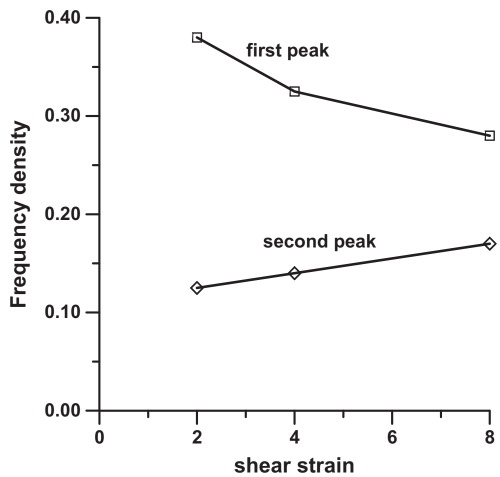

Fig. 12. Variations of the intensities of the peaks of the bimodal NNMD distributions shown in Fig. 10 as a function of strain.

$$\gamma = \frac{2}{tan(2\alpha)} \quad (8)$$

Fig. 9d shows the result of such strain analysis carried out on the three micrographs of Fig. 9. One can see that the shear is larger than the imposed average shear near the internal surface (6 vs. 4) while it is much less in the outer section (2 vs. 4).

The strain gradient is a consequence of the gradient in the shear stress. As discussed in Section 1 (see Eq. (5)), the shear stress varies only within a factor of 1.23 in the tube thickness for the present tube geometry and this ratio does not depend on the material. As shown in Ref. [11], the local shear stress is the same as the flow stress in HPTT because the axial stress does not contribute to the yield condition. Therefore, the relatively limited variation of the flow stress should not represent a major difficulty for the introduction of HPTT for tube processing and for structural applications of the obtained tubes. After all, it is the flow stress that puts limitations on the load bearing of a tube; the gradient in the plastic shear does not.

Fig. 10 displays quantitative measurements of the evolution of the grain size and the fraction of large-angle grain boundaries as a function of strain. The grain sizes were obtained by the linear intercept method in two directions: parallel ("length") and perpendicular to the shear direction ("width"). The grain boundary fraction was determined for two critical angles; for 5° and 15°. The 5° criterion eliminates subgrains while the 15° is only for HAGB. After the shear of 8, where homogenous ultra-fine structure appears within the whole thickness of the tube, the fraction of high-angle grain boundaries reaches almost 60%. A rapid evolution of the microstructure can be seen at a shear of $\bar{\gamma} = 2$ as the initial grain size before HPTT (~24 μm) drops down to 1.5 μm according to the linear intercept measure parallel to the shear direction. Further straining has two effects: first, it decreases both the width and the length of the grains (even though with a decreasing rate); and second, a more equiaxed grain morphology appears.

Toth et al. [26] suggested the use of next-neighbor misorientation density function (NNMD) to characterize the misorientation distribution of neighboring grains. Such a distribution can be calculated by assigning an average orientation to the grains that are identified by closed boundaries everywhere having a larger misorientation than a critical angle. Then the misorientation between two adjacent grains can be calculated from these average orientations. Such a distribution function provides useful information on the state of the grain subdivision process and differs significantly from the so-called pixel-to-pixel misorientation distribution which characterizes rather the lattice curvature instead of the grain structure. The NNMDs were also calculated in the present work and are displayed in Fig. 11 as a function of strain and position within the tube wall: near the inner surface (triangles, blue), in the middle (squares, red), and at the outer surface (circles, green). The distributions of the obtained NNMD functions are bimodal with a first peak

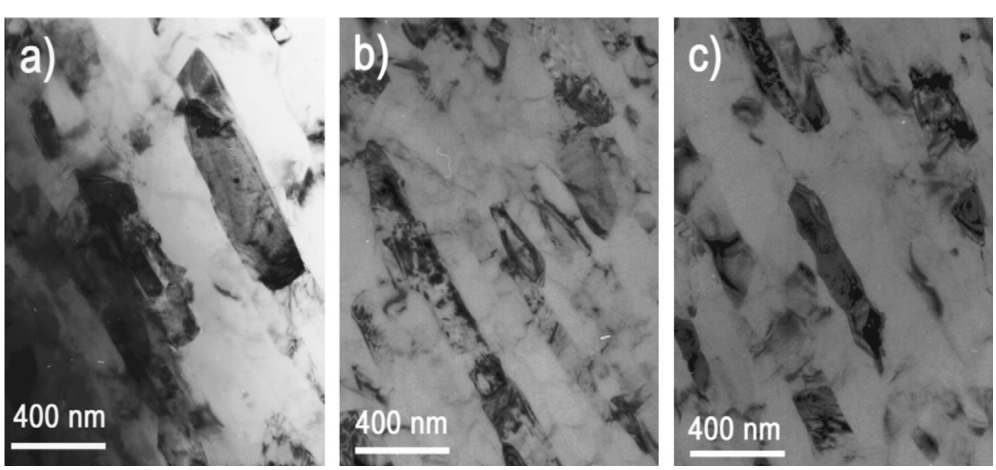

Fig. 13. Bright-field TEM images obtained in the AD plane (electron beam parallel to the tube axis) and showing the typical microstructure of the Al alloy processed by HPTT up to a shear strain of 20. The three images do correspond to different regions of the tube: outer part (a), center part (b) and inner part (c).

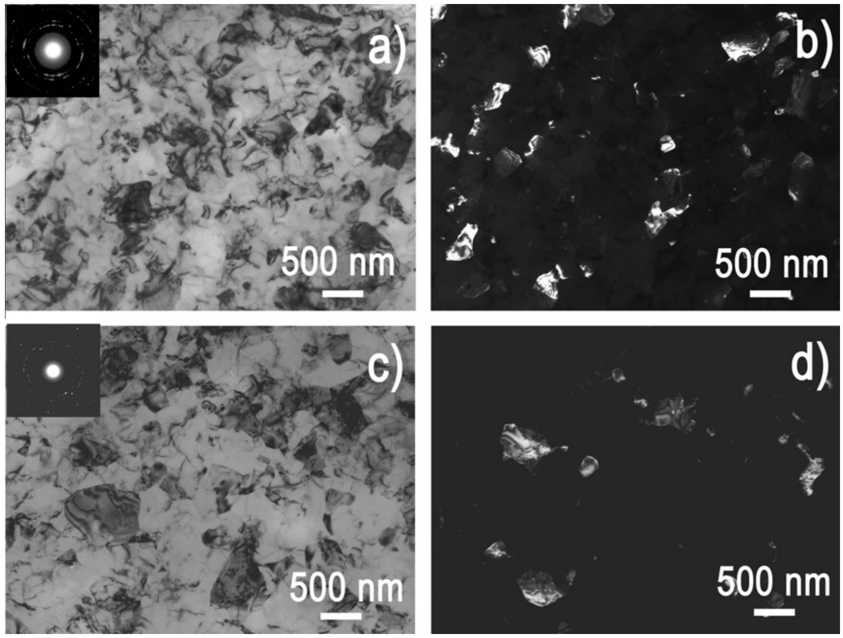

Fig. 14. TEM images obtained in the SD plane (electron beam parallel to the shear direction) and showing the typical microstructure of the Al alloy processed by HPTT up to a shear strain of 20. Images correspond to two different regions of the tube: the inner part (a and b) and the outer part (c and d). Images (a) and (c) are bright-field images with the electron diffraction pattern (insert); images (b) and (d) are the corresponding dark-field images obtained with an aperture selecting part of the two first Debye–Scherrer rings of the SAED.

at low angles of $\sim$12° and a second at high angles at 45°. At a given strain there are no systematic differences between the distributions with respect to the measurement position within the tube due to the measurement errors which are larger. Globally, the distribution tends to move toward high-angle grain boundaries as the deformation increases, i.e. the boundary misorientation distribution gets closer to the statistical prediction for a set of random orientations (Mackenzie distribution) but it still remains very distinct from random. The Mackenzie distribution is superposed on the graphs with dashed lines. Note that the Mackenzie distribution is between uncorrelated grain orientations while the present NNMD is a correlated misorientation distribution because it is made of misorientations of neighboring grains only.

The changes in the NNMDs can be further quantified by plotting the intensity variations of the two peaks as a function of strain; see Fig. 12. The intensity of the first peak decreases while the second one increases as a function of strain. This effect can be explained on the basis of the findings published in Ref. [26]. Namely, the first peak can be attributed to new grains that are neighbors in the interior of the original grains while the second one is due to the larger misorientations between new grains that are neighbors across the grain boundaries of the initial grains. The increase of this second population of grains is a result of the flattening of the initial grains during monotonic shear, which increases the relative proportion of grains sitting at the "old" grain boundaries. The first peak corresponds to relatively low misorientation angles because of its origin; these new grains are originating from the same initial orientation. Its intensity is decreasing mostly because of the increase of the intensity of the second peak; simply, the total integral of the frequency densities is always equal to 1. We can conclude then that the present experiments provide further evidences for the occurrence of the "geometrical" grain refinement process (i.e. the second peak), which makes a very large contribution to the increase of the fraction of large-angle boundaries during large strains.

Figs. 13 and 14 show TEM micrographs of the tube deformed to a mean shear strain of 20. The observations were made on two perpendicular planes: on the plane with normal AD (Fig. 13a–c) and on the plane with normal SD (Fig. 14a–d). On the AD plane a fairly uniformly spaced, parallel and nearly planar dense dislocation wall substructure can be seen. It is also important to note the low dislocation density inside nanoscaled grains and their smooth and straight boundaries.

The microstructure on the SD plane consists of ultrafine equiaxed grains, see Fig. 14a–d. Many strained contrasts are visible within grains, which can be related to lattice curvatures. Measurements from several dark-field images reveal that the grain size near to the inner surface of the tube is appreciably finer than at the outer surface. The mean grain sizes as determined by dark field images are $\sim$300 nm. The associated SAED patterns taken by using an aperture of 5 μm diameter are also shown in the figure. The SAED patterns have numerous reflections along Debye–Scherrer rings, indicating that the grain boundaries have high misorientation angles.

The present TEM analyses clearly demonstrate that the HPTT processing of CP Al results in a complete refinement

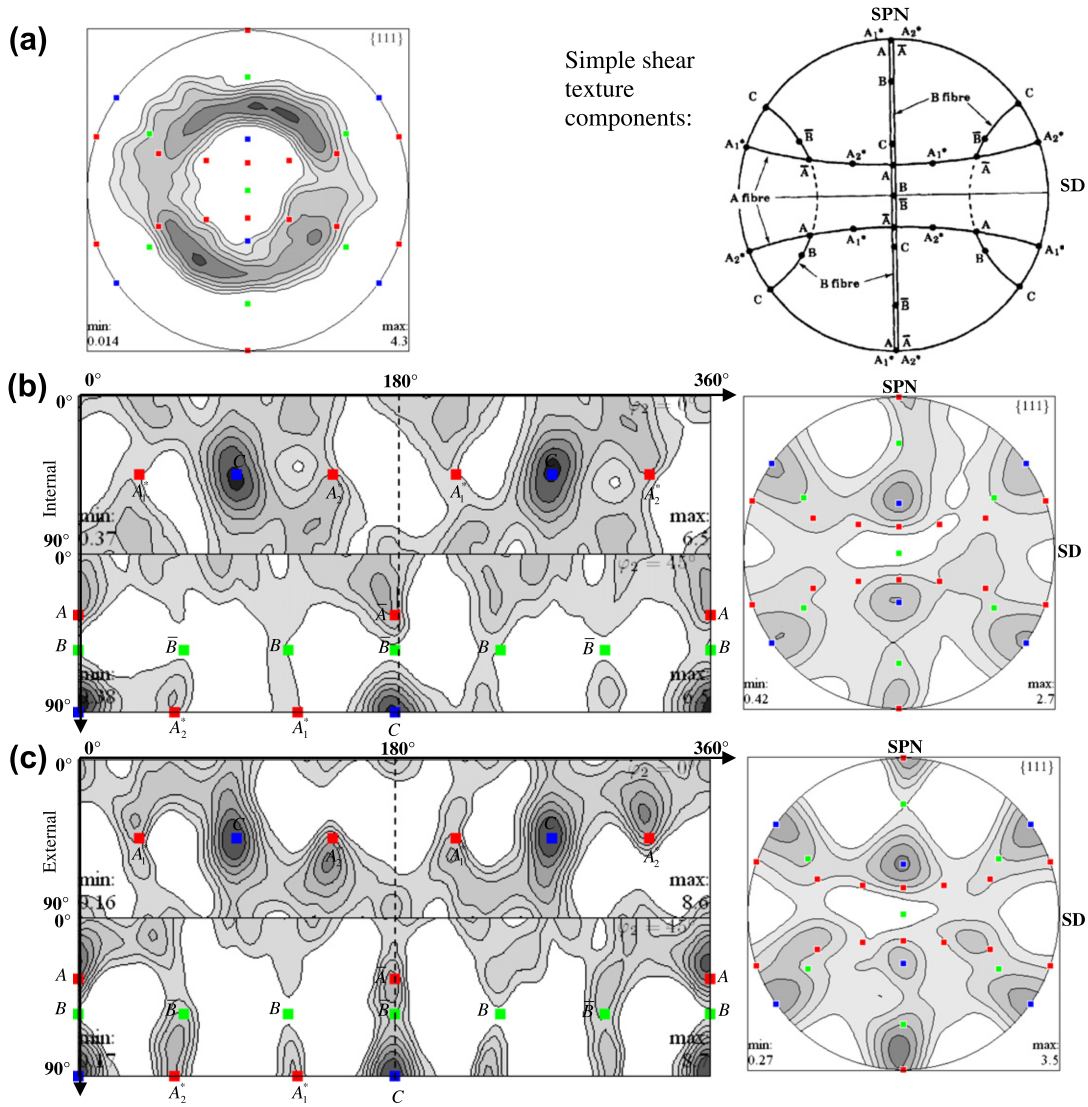

Fig. 15. The initial texture (a), and the textures at a shear of $\gamma = 2$ at the internal (b) and external (c) surfaces of the tube. The key figure for shear ideal orientations is also presented. Intensity levels of the textures: 0.7 1.0 1.4 2.0 2.8 4.0 5.6 (x random).

of the initial coarse-grained structures into an ultrafine-grained microstructure.

3.4. Evolution of crystallographic texture during HPTT

The CP Al used in this study had an initial relatively strong fiber texture resulting from the pre-forming extrusion process in which the $\langle 1\,0\,0\rangle$ fiber axis was parallel to the axis of the tube, see Fig. 15a. The deformation textures are shown in both orientation distribution function (ODF) and in $\{1\,1\,1\}$ pole figures for various conditions of straining and positions within the tube in Figs. 15–17. For the ODF, only the $\varphi_2 = 0°$ and $\varphi_2 = 45°$ sections are shown; these can display all ideal orientations of shear textures. Twofold sample symmetry is valid for shear textures (around the AD axis in the present HPTT testing); however, no sample symmetry was applied when processing the measured textures. Nevertheless, the obtained textures are not far from the expected sample symmetry; see the pole figures in Figs. 15–17.

Aluminum is a high stacking fault energy face-centered cubic (fcc) metal, thus its typical shear texture consists of a partial B fiber, with a much less strong A fiber [27]. Fig. 15 shows the textures at a shear of $\bar{\gamma} = 4$ on the inner and outer surfaces of the tube. In these textures the C component is the major one which is on the B fiber. The $B/\overline{B}$ components are practically absent in the texture of the internal face, but on the external surface $\overline{B}$ is stronger. The A fiber is present but with much less intensity than the B fiber. There is no major difference between the textures of the inside and outside regions of the tube although a gradient in strain must exist.

The textures at the shear of $\bar{\gamma} = 20$ are displayed in Fig. 16. One can see that the C component is further strengthened at the internal surface where the strain is expected to be larger. At the outer surface the texture is

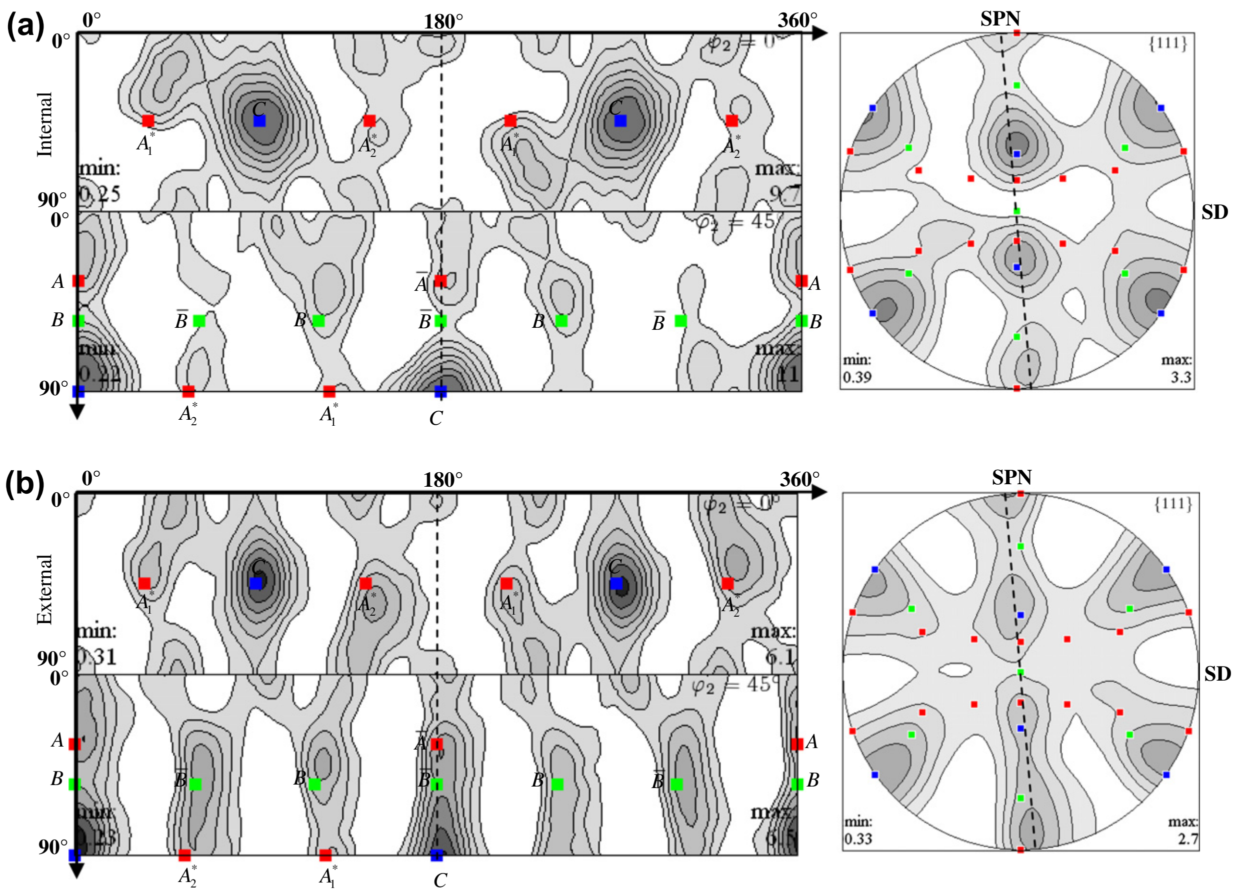

Fig. 16. HPTT textures at a shear of $\gamma = 20$ measured on the internal face (a) and on the external face (b) of the CP Al tube. Intensity levels: 0.7 1.0 1.4 2.0 2.8 4.0 5.6 (x random).

much weaker and the B fiber appears in more uniform distribution. An important feature of the textures at this very large strain is their tilt in the direction of shear (which was negative). Such rotations have widely been reported in shear textures [28–30]. Generally, there is anti-shear tilt at lower strains which can become a tilt in the direction of shear. A non-tilted texture can be observed at a strain of about $\bar{\gamma} = 4$ (Fig. 15).

The textures are presented at increasing strain in Fig. 17 taken at the internal surface of the tube. One can see that there is significant development both in intensities and in the relative proportion of the texture components. In order to follow the general strength of the texture, the texture index was calculated and plotted in Fig. 18a. As can be seen in this figure the strongest texture was the initial one, which was a {1 0 0}‖AD fiber texture. The texture strength first decreased by the formation of shear texture (shears of 2 and 4) then slightly increased (shears of 6 and 8), and finally it decreased to a relatively low value at the largest shear ($\bar{\gamma} = 20$). The variations in the intensities of the individual ideal orientations are plotted in Fig. 18b. Apart from the initial stage ($\bar{\gamma} = 2$), the most important texture component is always the C, which strengthens continuously with strain; it goes up to an intensity of 11 at the shear strain of 20. The second most important component of the textures are the $A/\bar{A}$, while a continuous increase in the intensity of $B/\bar{B}$ is also evident.

The tilt of the texture from its symmetry position in the sense of the shear becomes evident starting from a shear of 8. Such tilts were also observed in torsion of copper [30] and in torsion of Al [31]. Toth et al. attributed this effect to the strain rate sensitivity of slip [32], which permits orientations to cross the ideal positions in the direction of shear. The effect is only significant if the strain rate sensitivity index (m) is relatively high. In Ref. [32], the same amount of tilt was obtained by simulation for an m-value of 0.125 than in the present testing at large strains. It is actually reported that strain-rate sensitivity of fcc metals is increased due to the decrease in activation volume in the nanocrystalline regime [33]. As shown in the present experiment, the grain size is below 300 nm in the HPTT deformed CP Al starting from a shear of 4. This grain size is sufficiently low to obtain high strain rate sensitivity of the material, which can induce the tilts of the texture components due to the increased strain rate sensitivity of slip.

3.5. Comparisons to other techniques and limitations

The obtained experimental results clearly demonstrate that the HPTT process is a viable technique to obtain

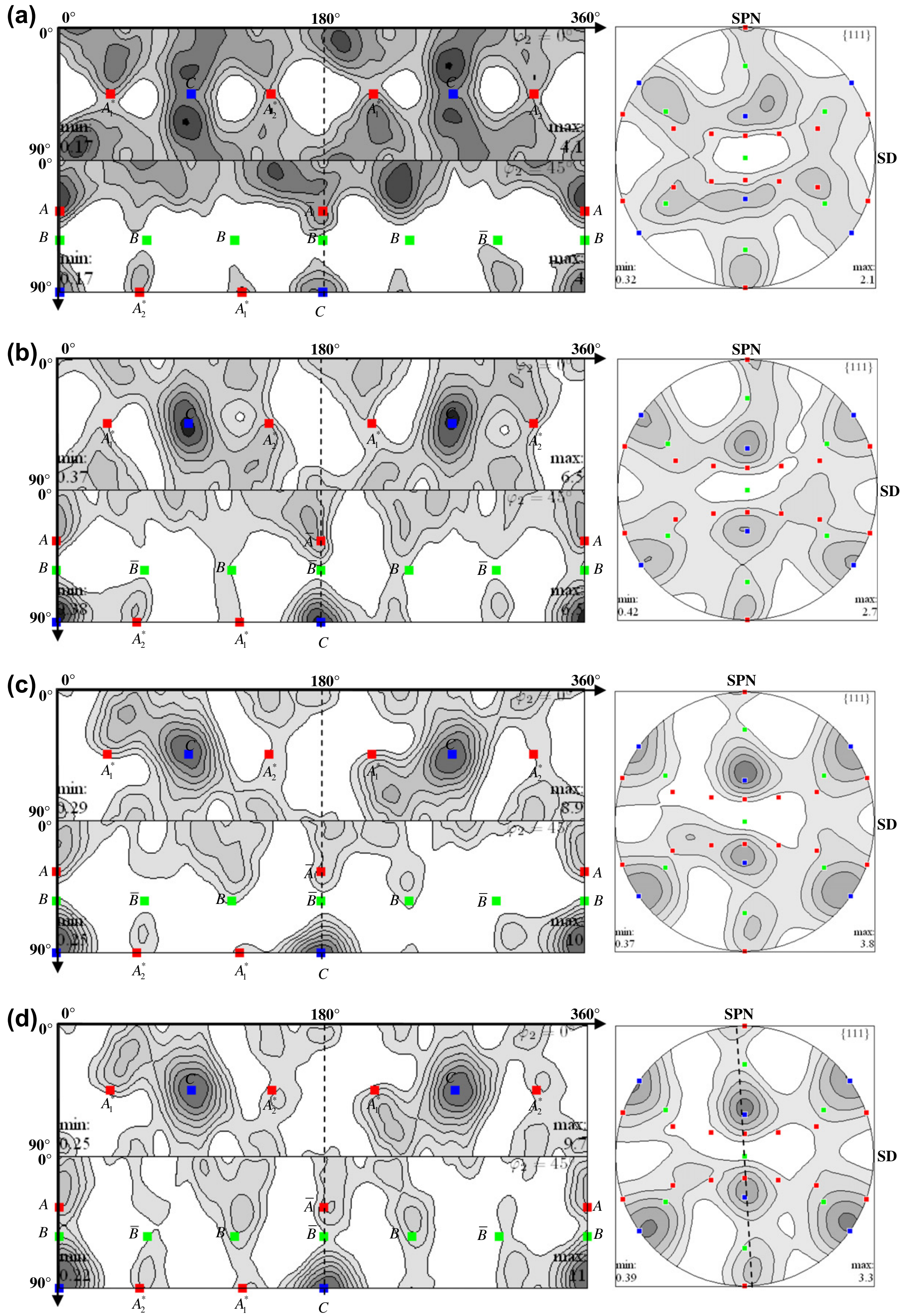

Fig. 17. Texture development on the internal face of the HPTT deformed Al tubes from shear of $\gamma = 2$ (a) through $\gamma = 4$ (b), $\gamma = 6$ (c) up to $\gamma = 8$ (d). Intensity levels: 0.7 1.0 1.4 2.0 2.8 4.0 5.6 (x random).

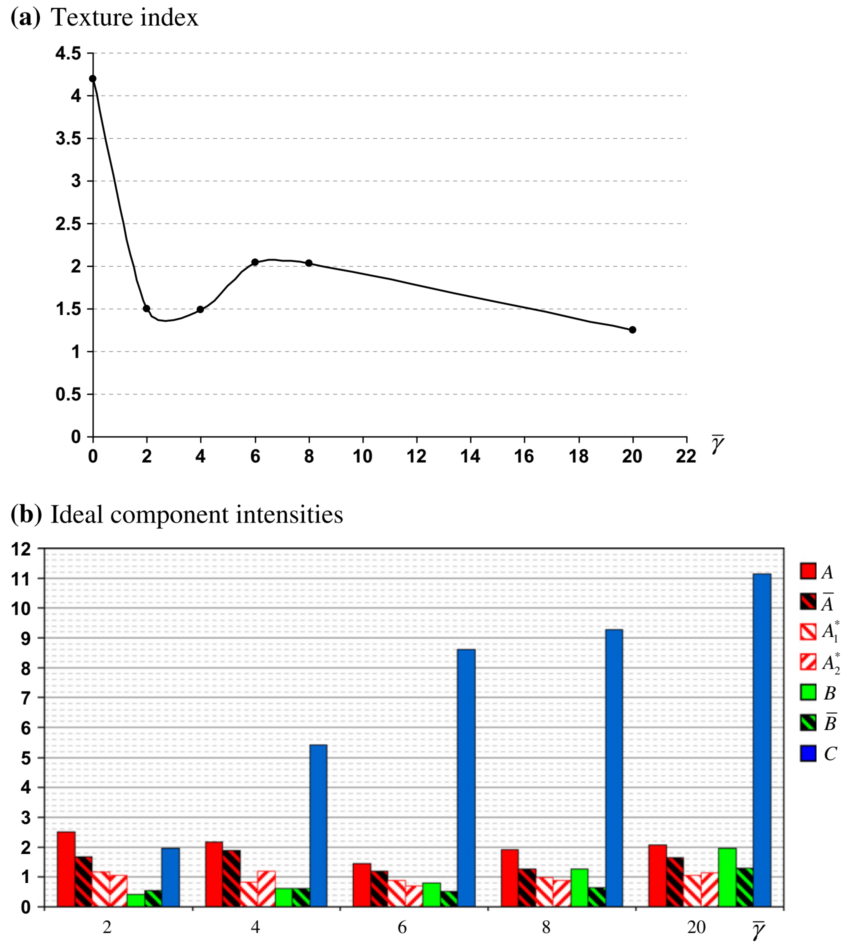

Fig. 18. (a) Variation of the texture index as a function of shear strain on the internal surface of CP Al tube processed by HPTT. (b) Evolution of the intensities of the ideal texture components as a function of shear (x random).

UFG microstructures. It has been found that the yield stresses increase significantly more than in the most applied SPD technique, excluding ECAP. Actually, it has been reported in Ref. [34] that after a shear of 2 and 4 in ECAP, CP Al had a shear yield stress of ~60 and 70 MPa, respectively, while in the present HPTT tests, CP Al strengthened up to 115 MPa and 144 MPa, respectively, at the same shear strains. However, as discussed in Section 3.2, the slope of Stage IV is just slightly larger in HPTT than in simple torsion. It is remarkable that after a shear of 8 in HPTT, the grain size is less than 0.5 μm, which was never observed in other SPD techniques in CP Al.

One has to mention, nevertheless, that HPTT has limitations concerning the length of the tube. The weak point of the process is the internal mandrel which has to bear the imposed external torque. The external applied torque is loading the cross-section of the internal mandrel. A linear stress distribution is valid within the internal mandrel with a maximum yield stress τ_0^m at its outer radius. We can write the following inequality for the developed torques to ensure that the mandrel does not break:

$$\int_0^a 2r\pi \frac{r}{a}\tau_0^m r\,dr \leqslant \int_0^h 2a\pi\tau_0^t a\,dh \tag{9}$$

Here τ_0^t is the yield stress of the tube at its internal radius. After integration we obtain:

$$\frac{h}{D} \leqslant \frac{1}{8}\frac{\tau_0^m}{\tau_0^t} \tag{10}$$

where D is the diameter of the tube. This means that the length-to-diameter ratio has to be less than 1/8 if the yield stresses of the mandrel and the tube are the same. Or, for a ratio of 1 (tube diameter is equal to its length), the mandrel's yield strength has to be eight times larger.

4. Conclusions

This investigation provides the first comprehensive report about the mechanical and microstructural characteristics of CP aluminum processed by the new HPTT severe plastic deformation technique. The most interesting feature of HPTT is that very high plastic strains can be applied on a tube in one single operation. Although limited in length, the deformed tubes can have relatively large dimensions, easing in this way the experimental characterization of the samples for their mechanical properties, for their microstructures as well as for texture investigations. An existing HPT machine can be relatively easily converted into an HPTT machine; only the die has to be changed. From the results obtained in the present investigation, the following major conclusions can be drawn.

1. The new HPTT process is a viable new severe plastic deformation technique which was successfully applied to deform CP Al tubes up to shears of 24. Ultra-fine-grained microstructures were obtained with grain sizes of $\sim$300 nm.
2. The ring-hoop test was applied for testing tensile properties of the deformed tubes. The mechanical characteristics of HPTT deformed tubes showed superior flow stress with respect to the initial material. It was also shown that the axial force during HPTT does not contribute to the plastic flow of the material; it is only controlled by the shear component of the applied stress.
3. The microstructure examinations using the EBSD technique showed a bimodal misorientation distribution between the neighboring grains which was attributed to "internal" and "grain-boundary" new grains originating from the initial grains. This result indicates that geometrical grain refinement is an important element of the grain fragmentation process at large strains.
4. The textures measured in the HPTT deformed tubes are typical shear textures. At very large strains the texture appears with small tilt in the sense of the shear with respect to its ideal position, which is due to the increased strain rate sensitivity of slip. The main texture component is the C component, which continuously strengthens with strain.

Acknowledgement

The authors are grateful to Prof. A.D. Rollett (Carnegie Mellon University, Pittsburgh) for valuable discussions on strain hardening. This work was carried out within the framework of an ANR project (ANR "HYPERTUBE") of the French National Research Agency.

References

[1] Valiev RZ, Estrin Y, Horita Z, Langdon TG, Zehetbauer MJ, Zhu YT. JOM 2006;58:33.
[2] Valiev RZ, Krasilnikov NA, Tsenev NK. Mater Sci Eng A 1991;137:35.
[3] Valiev RZ, Tsenev NK. In: Langdon TG, Merchant HD, Morris JG, Zaidi MA, editors. Hot deformation of aluminum alloys. Warrendale (PA): The Minerals, Metals and Materials Society; 1991. p. 319.
[4] Valiev RZ, Korznikov AV, Mulyukov RR. Mater Sci Eng A 1993;168:141.
[5] Valiev RZ, editor. Ultrafine-grained materials prepared by severe plastic deformation: special issue. Ann Chim Sci Mater 1996;21:369.
[6] Languillaume J, Chmelik F, Kapelski G, Bordeaux F, Nazarov AA, Canova G, et al. Acta Metall Mater 1993;41:2953.
[7] Saito Y, Utsunomiya H, Tsuji N, Sakai T. Acta Mater 1999;47:579.
[8] Cao Y, Wang YB, Figueiredo RB, Chang L, Liao XZ, Kawasaki M, et al. Acta Mater 2011;59:3903.
[9] Toth LS, Arzaghi M, Fundenberger J-J, Beausir B, Bouaziz O, Arruffat-Massion R. Scripta Mater 2009;60:175.
[10] Zangiabadi A, Kazeminezhad M. Mater Sci Eng A 2011;528:5066.
[11] Lowe TC, Valiev RZ. JOM 2004;56:64.
[12] Valiev RZ, Langdon TG. Adv Eng Mater 2010;12:677.
[13] Bridgman PW. Phys Rev 1935;48:825.
[14] Pougis A, Toth LS, Bouaziz O, Fundenberger JJ, Barbier D, Arruffat R. Scripta Mater 2012;66:773.
[15] Wang H, Bouchard R, Eagleson R, Martin P, Tyson WR. J Testing Eval 2002;30:382.
[16] Humphreys FJ. J Mater Sci 2001;36:3833.
[17] Nadai A, Davis E. J Appl Phys 1937;8:205.
[18] Zehetbauer MJ, Stuwe HP, Vorhauer A, Schafler E, Kohout J. Adv Eng Mater 2003;5:330.
[19] Song Y, Yoon EY, Lee DJ, Lee CS, Kim, HS. Oral lecture at the BNM2011 conference (Bulk Nanostructured Materials), UFA, August 23–26, 2011.
[20] Iwahashi Y, Horita Z, Minoru N, Langdon TG. Metal Mater Trans A 1998;29:2503.
[21] Sun PL, Yu CY, Kao PW, Chang CP. Scripta Mater 2005;52:265.
[22] Yu CY, Kao PW, Chang CP. Acta Mater 2005;53:4019.
[23] El-Danaf EA, Soliman MS, Almajid AA, El-Rayes MM. Mater Sci Eng A 2007;458:226.
[24] Rollett AD. Strain hardening at large strains in aluminum alloys. Ph.D. thesis. Drexel University; 1988.
[25] Canova GR, Kocks UF, Jonas JJ. Acta Metall 1984;32:211.
[26] Toth LS, Beausir B, Gu CF, Estrin Y, Scheerbaum N, Davies CHJ. Acta Mater 2010;57:6706.
[27] Kocks UF, Tome CN, Wenk HR. Texture and anisotropy: preferred orientations in polycrystals and their effect on materials properties. Cambridge: Cambridge University Press; 1998.
[28] Beyerlein IJ, Li S, Necker CT, Alexander DJ, Tome CN. Philos Mag 2005;85:1359.
[29] Toth LS, Arruffat-Massion R, Germain L, Baik SC, Suwas S. Acta Mater 2004;52:1885.
[30] Toth LS, Jonas JJ, Daniel D, Bailey JA. Textures Microstruct 1992;19:245.
[31] Montheillet F, Cohen M, Jonas JJ. Acta Metall 1984;32:2077.
[32] Toth LS, Gilormini P, Jonas JJ. Acta Metall 1988;36:3077.
[33] Meyers MA, Mishra A, Benson DJ. Prog Mater Sci 2006;51:427.
[34] Kim KJ, Yang DY, Yoon JW. Mater Sci Eng 2010;527:7927.